ENVIRONMENTAL RESEARCH
LETTERS

LETTER • OPEN ACCESS

Canopy cover and microtopography control precipitation-enhanced thaw of ecosystem-protected permafrost

To cite this article: Joel F Eklof *et al* 2024 *Environ. Res. Lett.* **19** 044055

IOP Publishing Environ. Res. Lett. 19 (2024) 044055 https://doi.org/10.1088/1748-9326/ad31d7

ENVIRONMENTAL RESEARCH
LETTERS

OPEN ACCESS

RECEIVED
31 October 2023

REVISED
6 February 2024

ACCEPTED FOR PUBLICATION
8 March 2024

PUBLISHED
28 March 2024

LETTER

Canopy cover and microtopography control precipitation-enhanced thaw of ecosystem-protected permafrost

Joel F Eklof[1,*], Benjamin M Jones[2], Baptiste Dafflon[3], Élise G Devoie[4], Katie M Ring[1], Marie E English[1], Mark P Waldrop[5] and Rebecca B Neumann[1]

[1] Civil and Environmental Engineering, University of Washington, Seattle, WA, United States of America
[2] Institute of Northern Engineering, University of Alaska Fairbanks, Fairbanks, AK, United States of America
[3] Earth and Environmental Sciences Area, Lawrence Berkeley National Laboratory, Berkeley, CA, United States of America
[4] Department of Civil Engineering, Queen's University, Kingston, ON, Canada
[5] United States Geological Survey, Menlo Park, CA, United States of America
[*] Author to whom any correspondence should be addressed.

E-mail: jeklof@uw.edu

Keywords: permafrost, ecosystem-protected, active layer, advective heat transport, precipitation, talik, thermal conductivity

Supplementary material for this article is available online

Abstract

Northern high-latitudes are projected to get warmer and wetter, which will affect rates of permafrost thaw and mechanisms by which thaw occurs. To better understand the impact of rain, as well as other factors such as snow depth, canopy cover, and microtopography, we instrumented a degrading permafrost plateau in south-central Alaska with high-resolution soil temperature sensors. The site contains ecosystem-protected permafrost, which persists in unfavorable climates due to favorable ecologic conditions. Our study (2020–2022) captured three of the snowiest years and three of the four wettest years since the site was first studied in 2015. Average thaw rates along an across-site transect increased nine-fold from 6 ± 5 cm yr^{-1} (2015–2020) to 56 ± 12 cm yr^{-1} (2020–2022). This thaw was not uniform. Hummock locations, residing on topographic high points with relatively dense canopy, experienced only 8 ± 9 cm yr^{-1} of thaw, on average. Hollows, topographic low points with low canopy cover, and transition locations, which had canopy cover and elevation between hummocks and hollows, thawed 44 ± 6 cm yr^{-1} and 39 ± 13 cm yr^{-1}, respectively. Mechanisms of thaw differed between these locations. Hollows had high warm-season soil moisture, which increased thermal conductivity, and deep cold-season snow coverage, which insulated soil. Transition locations thawed primarily due to thermal energy transported through subsurface taliks during individual rain events. Most increases in depth to permafrost occurred below the ∼45 cm thickness seasonally frozen layer, and therefore, expanded existing site taliks. Results highlight the importance of canopy cover and microtopography in controlling soil thermal inputs, the ability of subsurface runoff from individual rain events to trigger warming and thaw, and the acceleration of thaw caused by consecutive wet and snowy years. As northern high-latitudes become warmer and wetter, and weather events become more extreme, the importance of these controls on soil warming and thaw is likely to increase.

1. Introduction

Permafrost covers approximately 24% of the terrestrial landscape of the Northern Hemisphere (Brown *et al* 1997). Atmospheric temperatures in the Northern Hemisphere have warmed faster than the global average, and this amplified warming is expected to strengthen in the future (Rantanen *et al* 2022). Trends in permafrost temperature are consistent with trends in atmospheric temperature, with widespread warming observed since 1980 (Smith *et al* 2022). However, other environmental factors, such as vegetation, soil properties, hydrology, topography, local climate, and snow, also regulate permafrost temperature and thaw progression (Engstrom *et al* 2005, Shur and Jorgenson 2007, O'Donnell *et al* 2009, Blok *et al* 2011, Juszak *et al* 2014, Loranty *et al* 2018, Smith *et al* 2022).

Rainfall is one such environmental factor that contributes to permafrost dynamics. Rainfall can accelerate permafrost thaw through advective heat transport (Iijima *et al* 2010, Connon *et al* 2018, Devoie *et al* 2019, 2021, Douglas *et al* 2020, Mekonnen *et al* 2021, Magnússon *et al* 2022) and by increasing soil thermal conductivity (Farouki 1981, Hinkel and Nelson 2003, Subin *et al* 2013), but rain can also slow thaw since wetter soils require more energy to warm due to greater heat capacity (Farouki 1981, Hinkel *et al* 2001, Subin *et al* 2013, Clayton *et al* 2021) and experience increased evaporative cooling (Hamm and Frampton 2021). Northern high-latitude precipitation is expected to increase (Bintanja and Selten 2014, Bintanja *et al* 2020), which may enhance the role of rain in permafrost progression.

We hypothesize that ecosystem-protected permafrost, the warmest and most vulnerable of the permafrost classes, will be most sensitive to these changes. Ecosystem-protected permafrost is located in regions with a mean annual air temperature (MAAT) above 0 °C where permafrost persists in unfavorable climates due to favorable ecologic conditions (Shur and Jorgenson 2007). Understanding how ecosystem-protected permafrost degrades is crucial because ecosystem-protected permafrost acts as a forecaster and predictor of future thaw in more northern latitudes (Beilman *et al* 2001) which are becoming more climatically similar to existing ecosystem-protected areas (Cohen *et al* 2014, Kusunoki *et al* 2015, Liu *et al* 2021, Wang *et al* 2021, Rantanen *et al* 2022, Thackeray *et al* 2022). Degradational features such as taliks are common in these warm permafrost systems (Harris 1988, Connon *et al* 2018, Devoie *et al* 2019). Taliks are layers of year-round unfrozen ground that have been shown to enhance permafrost thaw. One potential mechanism is the enhancement of advective heat transport with rain by providing subsurface lateral flow paths for runoff (Connon *et al* 2018, Devoie *et al* 2019, 2021).

To better understand the impact of rain, as well as other environmental factors affecting permafrost in the ecosystem-protected zone, we instrumented a rapidly degrading permafrost plateau in south-central Alaska with high-resolution soil temperature sensors and measured environmental variables including canopy cover, snow, and microtopography. Our study took place from 2019 to 2022 and contained the wettest and snowiest years on record since 2015.

2. Methods

2.1. Site description

The site is located in the western Kenai Peninsula lowlands (60.47° N, −150.73° W) (figures 1(A) and (B)) within Kenai National Wildlife Refuge (permit: 2018-Res-RBNeumann-6276). Fieldwork took place May 2019 to September 2022. The plateau is surrounded by and contains wetland features (figure 1(C)) and experiences a semi-continental climate due to Cook Inlet to the northwest, Kachemak Bay to the south, and its location within the rain shadow of the Kenai mountains to the east. Plateau and wetland soil is peat-dominated to 3 m depth (Jones *et al* 2016). In 2015, the average seasonally frozen ground thickness was 45 cm, which overlayed continuous taliks (Jones *et al* 2016). Average depth to permafrost measured in 2015 was 1.37 m with an average permafrost thickness of 5.61 m (Jones *et al* 2016). Black spruce trees (*Picea mariana*) grow on the most elevated sections (hummocks) of the permafrost plateau (figure 1(D)). Plateau lowland areas (hollows) contain no live trees.

2.2. Soil temperature measurements

Soil temperatures were measured using 160 cm long Distributed Temperature Profilers (DTPs) with sensors every 10 cm (Dafflon *et al* 2022, Wielandt *et al* 2023) installed in August 2020. DTPs have an accuracy of ±0.05 °C and a 15 min measurement interval. Data were depth-corrected annually for frost heave and subsidence and linearly interpolated for location-to-location consistency.

2.3. Geospatial measurements and relative-elevations

A digital elevation model was created in MATLAB (R2022b) using 1620 real-time kinematic points recorded using Emlid Reach RS2 units in November 2020 (figure 1(E)). Relative-elevations were determined by comparing DTP elevations to the average elevation of the surrounding 5 m radius area. Relative-elevations were used to define locations as a hummock, transition, or hollow (figures 1(C) and (E)). Hummock locations were >0.2 m above, transition locations were between 0.2 m above and 0.1 m below, and hollow locations were >0.1 m below their surroundings (figure 1(E)).

2.4. Meteorological measurements and data

Precipitation was measured with an annually calibrated HOBO Rain Gauge installed April 2019 in a 5 m clearing. Air temperature was recorded with a HOBO Temperature/RH Logger installed April 2019 using dense black spruce as a radiation shield (Lundquist and Huggett 2008). Data were gap-filled using two National Weather Service stations, COCOAKKP7 and COOPKEYA2, located within 6 km (NOAA 2023). Air temperature and precipitation data from 2015 to 2019 were sourced from interagency weather station SDFA2 located 16 km west. Trends in SDFA2 data were consistent with in situ meteorological measurements recorded during the study period. Snow depth was measured with an avalanche probe in March 2022. Snow water equivalent data were sourced from Moose Pen SNOTEL site 32 km northeast (USDA 2023). Cumulative shortwave radiation was calculated using HPEval, a MATLAB-based software

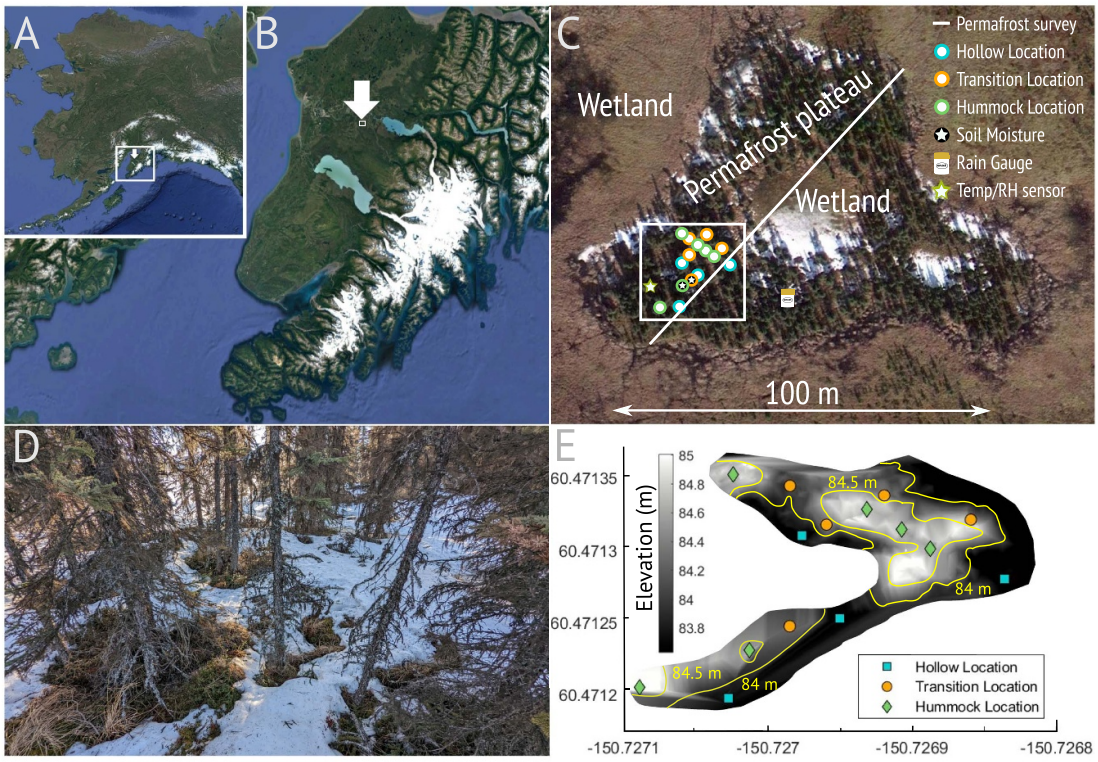

Figure 1. Site overview. (A) Alaska map with an inset of the Kenai Peninsula shown in panel (B). (B) Kenai Peninsula map with an arrow indicating an inset of the site location shown in panel (C). (C) A Google Earth image of the site with an inset of our core instrumentation area shown in panel (E). Instrumented high-elevation (hummock) locations are green, mid-elevation (transition) locations are orange, and low-elevation (hollow) locations are light blue. Wetland and permafrost areas along with rain gauge, temperature/RH sensor, and two soil moisture sensor locations are labeled. The across-site permafrost transect is shown as a white line. (D) A field photo of plateau topography and snow cover heterogeneity. (E) A digital elevation model of our core instrumentation area. Shapes denote the instrumented locations shown in the inset of panel (C). Yellow topographic contour lines label every 0.5 m of elevation change. Names and locations of individual DTPs are shown in SI figure S4.

tool that uses high-resolution hemispherical photos to estimate shortwave radiation below forest canopy (Jonas *et al* 2020).

2.5. Hydrologic measurements

In-Situ pressure transducers and barometer were deployed in fully-screened PVC wells annually from May to September (2019–2022). Sensor data were verified with manual groundwater measurements taken 2–3 times annually between May and September with a Solinst Water Level Meter. Soil moisture was measured continuously at one hummock (90 cm length sensor) and one transition (120 cm length sensor) location (figure 1(C)) using GroPoint Multi-Depth Soil Moisture Sensors attached to GroPoint Data Loggers installed in August 2020. Profilers measured a composite value of percent water every 15 cm along the length of the sensor at a 30 min interval. Outputs were calibrated for peat soils (Yoshikawa *et al* 2004) and a manufacturer-provided dielectric correction (1.019) was applied for $\leqslant 0$ °C soils.

2.6. Thermal conductivity modeling

Soil thermal conductivity was estimated using a physically-based model (Zhao *et al* 2019) that used degree of saturation, dry thermal conductivity, and wet thermal conductivity as inputs. Degree of saturation was calculated by normalizing measured water content by the highest observed water content, 96.7%. Dry and wet thermal conductivities were estimated through weighted averages of the thermal conductivities of air (0.025 W m^{-1} K^{-1}), water (0.579 W $m^{-1}K^{-1}$ at 10 °C), and organic matter (~0.074 W $m^{-1}K^{-1}$). Dry thermal conductivity (0.027 W $m^{-1}K^{-1}$) assumed 96.7% air and 3.3% organic matter. Wet thermal conductivity (0.562 W $m^{-1}K^{-1}$) assumed 96.7% water and 3.3% organic matter. For $\leqslant 0$ °C soils, we calculated thermal conductivities assuming no ice content and maximum possible ice content. Maximum ice content was estimated as the difference between the current and highest observed water content of the measurement location. The thermal conductivity of 0 °C ice is 2.22 W $m^{-1}K^{-1}$.

2.7. Canopy measurements

Canopy cover percentage was determined through image analysis of upward-facing smartphone photos taken with a Moment 14 mm fisheye lens 1 m above the soil surface in July 2022. Photos were analyzed in ImageJ by cropping the photo into a circle,

splitting the photo into color panes, thresholding the blue pane into sky and vegetation pixels, and calculating percent cover from the relative proportion of pixels (Beckschäfer 2015).

2.8. Depth to frost table measurements

Permafrost table depth was estimated annually through manual probing. Probe length was 2.2 m from 2019–2021 and extended to 3.1 m in 2022. Measurements took place annually in mid-September. DTP location probing included four replicates within a 30 cm radius. Across-site transect (figure 1(C)) probing included three replicates, mimicking the methods and locations of Jones *et al* (2016).

2.9. Statistical methods

Environmental variables and thermal response metrics were compared for hummock, transition, and hollow locations using one-way ANOVA followed by Tukey HSD post-hoc using $\alpha = 0.05$. Data were $\log_{10}$ transformed to increase normality and reduce skew before ANOVA analysis. Data presented in figures are shown in non-transformed space for visual clarity. Correlations were determined by fitting data with a linear regression model and using two-sided hypothesis testing with $\alpha = 0.05$.

3. Results

3.1. Site meteorological conditions

From 2015 to 2022, MAAT was +3.3 °C with a mean annual precipitation of 480 mm (NOAA 2023). From 2020 to 2022, the site experienced the three snowiest years (figure 2(A)) and the second, third, and fourth wettest years (figure 2(B)) since 2015. Average air temperature did not vary significantly (SI figure S1). Three large warm-season rain events, defined as events with >50 mm of rain over two weeks, took place during our study in July 2020 (58 mm), July 2021 (54 mm), and July 2022 (77 mm) (figure 2(B-i,ii). The July 2020 event took place before the installation of site DTPs and soil moisture profilers and was therefore not included in further analyses.

3.2. Permafrost degradation along the across-site transect

Permafrost thaw rates accelerated during the study period (2020–2022) relative to preceding years (2015–2020). In the time between depth to permafrost measurements by Jones *et al* (2016) in 2015 and our measurements in 2020, the permafrost table along the across-site transect (figure 1(C)) deepened 32 ± 25 cm, or 6 ± 5 cm yr^{-1}, on average (figure 3). Between 2020 and 2022, the permafrost table deepened 112 ± 37 cm or 56 ± 18 cm yr^{-1} (figure 3), a nine-fold increase in annual thaw rate compared to 2015–2020. Documented thaw occurred below the base of the seasonally frozen layer, and therefore, expanded existing taliks.

3.3. Environmental variables within microtopographic groups

Among 14 instrumented locations, five were categorized as hummock, four as hollow, and six as transition locations. The three groups had significantly different relative-elevations (figure 4(A), $p < 0.001$). Average canopy cover of hummock, transition, and hollow locations was 77 ± 7%, 65 ± 14%, and 58 ± 7%, respectively. Percent coverage was only statistically different between hummock and hollow locations (figure 4(B), $p < 0.05$). Average snow depth of hummock, transition, and hollow locations was 8 ± 10 cm, 18 ± 13 cm, and 35 ± 12 cm, respectively. Snow depth was only statistically different between hummock and hollow locations (figure 4(C), $p < 0.05$). Shortwave radiation and moss depth did not significantly differ among groups (SI Fig. S2). Snow depth had significant negative correlations with relative-elevation (figure 4(D), $p < 0.05$) and canopy cover (figure 4(E), $p < 0.05$). Canopy cover and relative-elevation were significantly correlated (SI figure S2).

3.4. Permafrost and subsurface temperature regimes within microtopographic groups

Hummock locations had significantly shallower depths to the permafrost table (figure 5(A), $p < 0.001$) and significantly slower rates of annual permafrost thaw (figure 5(B), $p < 0.05$) than transition and hollow locations. In 2022, average depth to permafrost at hummock locations was 97 ± 39 cm compared to 252 ± 53 cm and 288 ± 15 cm at transition and hollow locations, respectively. Average annual thaw rates between 2020 and 2022 at hummock locations were 8 ± 9 cm yr^{-1} compared to 39 ± 13 cm yr^{-1} and 44 ± 6 cm yr^{-1} at transition and hollow locations, respectively.

At a depth of 10 cm, cold-season soil temperatures of hummock locations were significantly colder (−3.5 ± 1.7 °C) than hollow locations (−0.6 ± 0.4 °C), while transition locations (−1.7 ± 1.1 °C) were statistically indistinguishable from either group (figure 5(C), $p < 0.05$). A comparison depth of 10 cm was chosen to maximize sensitivity to surface-atmosphere interactions while avoiding diel temperature oscillations. In hummock and transition locations, freezing temperatures (−0.05 °C) reached significantly deeper depths of 28 ± 11 cm and 20 ± 11 cm, respectively, than in hollow locations where −0.05 °C reached a depth of 3 ± 6 cm (figure 5(E), $p < 0.001$). A threshold of −0.05 °C was used to track extent of freezing since DTPs have a confidence interval of ±0.05 °C.

Hummock locations were significantly cooler (5.2 ± 1.7 °C) than hollows (9.1 ± 0.7 °C) during the warm-season at 10 cm depth, while temperatures at transition locations (7.9 ± 0.4 °C) were statistically indistinguishable from either group (figure 5(D),

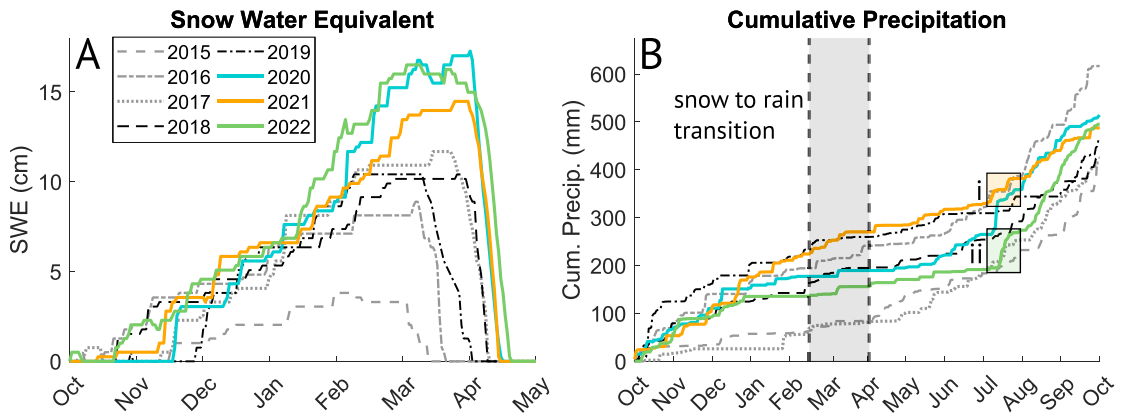

Figure 2. Meteorological forcing from 2015 to 2022. Line graphs show stacked annual time series of (A) snow water equivalent and (B) cumulative precipitation. Data for 2020 is blue, 2021 is orange, and 2022 is green. Data from 2015–2019 are gray or black with varied line styles displayed in the legend. The snow-to-rain transition period is shown as a gray box in Panel (B). Black-bordered orange (i) and green (ii) boxes in Panel (B) show periods of intense rain during July 2021 and 2022, respectively.

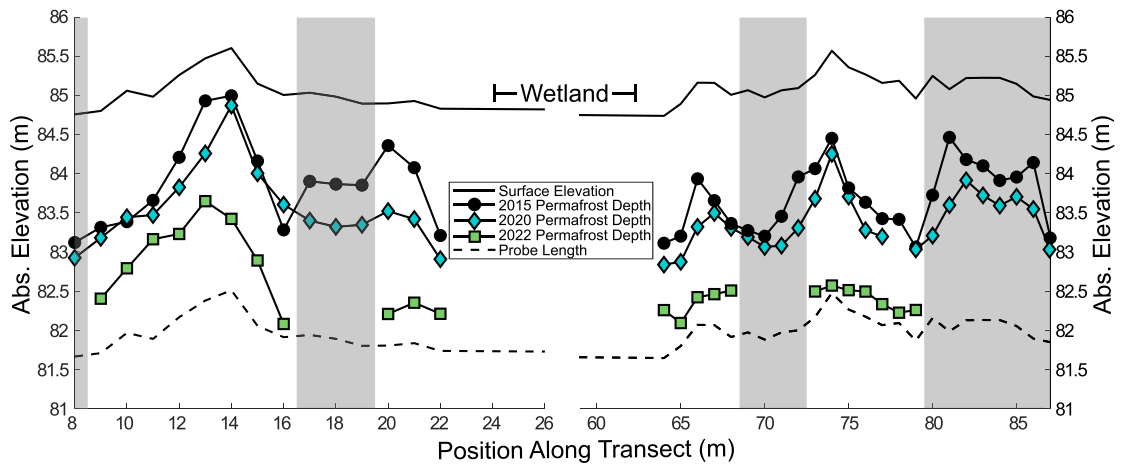

Figure 3. Permafrost thaw along the across-site transect shown in figure 1(C). Depths to the permafrost table measured in 2015 by Jones *et al* (2016) are shown as black circles. Our measurements from September 2020 and September 2022 are shown as blue diamonds and green squares, respectively. Surface elevation is marked with a thin solid black line based on data from Jones *et al* (2016). Maximum probe depth is marked with a dashed black line. Gray vertical bars label locations that had permafrost deeper than our 3.1 m probe in 2022. Wetland locations (positions 23-63) are labeled.

$p < 0.05$). In hummock locations, warm temperatures (+3 °C) only reached a depth of 20 ± 17 cm, while in transition and hollow locations, warm temperatures reached depths of 69 ± 33 cm and 101 ± 9 cm, respectively. The depth of warming in hummock locations was significantly shallower than that of transition and hollow locations (figure 5(F), $p < 0.05$). A threshold of +3 °C was the warmest temperature that did not penetrate beyond the 160 cm sensor length of any location.

3.5. Thermal and hydrologic responses to large rain events

Large rain events (>50 mm) occurred in July 2021 and 2022 (figure 2(B)). During these events, a greater thickness of the soil column at transition locations warmed from ⩽0 °C to above-freezing temperatures than at hummock or hollow locations in both 2021 (figure 6(A), $p < 0.01$) and 2022 (figure 6(B), $p < 0.01$). During the 2021 rain event, an average of 107 ± 20 cm of soil within transition locations warmed from ⩽0 °C to >0 °C compared to 31 ± 42 cm and 6 ± 4 cm of soil in hollow and hummock locations, respectively (figure 6(A)). A similar thickness of transition soil warmed from ⩽0 °C to >0 °C during the 2022 rain event, 106 ± 14 cm, compared to <1 cm and 10 ± 1 cm of soil in hollow and hummock locations, respectively (figure 6(B)). The observed thickness of transition-location warming and thaw that occurred during both rain events (106–107 cm) included over 40% of total above-permafrost soil during both years (252 ± 53 cm) (figures 5(A) and 6). Smaller warm-season rain events did not cause notable warming.

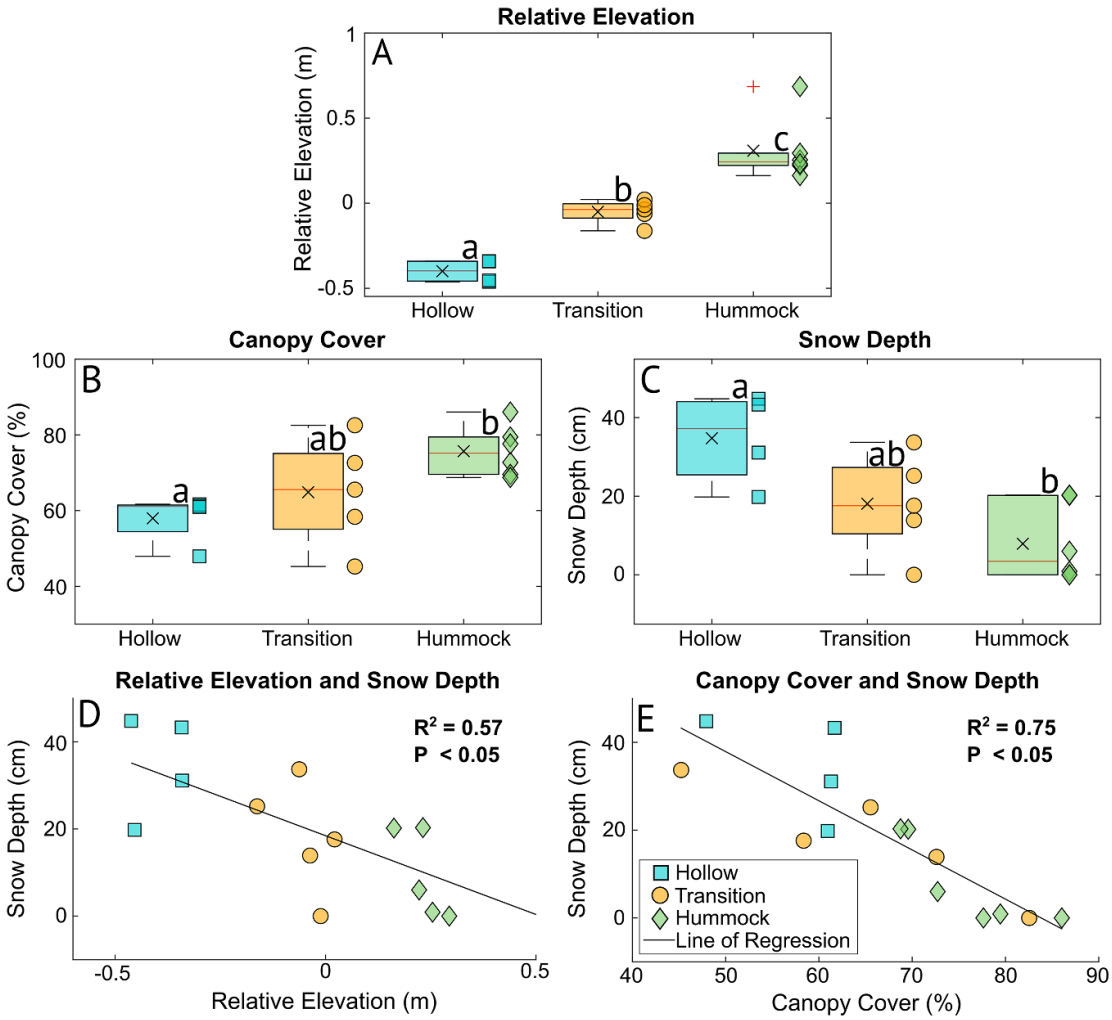

Figure 4. Environmental variables across the site. (A)–(C) Box and whisker plots showing: (A) relative-elevation of sensor locations, (B) canopy percentage, and (C) snow depth. On each box plot, the central line indicates the median, 'x' marks the mean, edges of the box indicate the 25th and 75th percentiles, whiskers indicate the most extreme non-outlier data points, and a red plus marker indicates an outlier greater than 2.7 standard deviations from the mean. Letters on top of boxes indicate data sets with statistically significant differences in mean as determined through one-way ANOVA. (D), (E) Scatter plots showing: (D) snow depth versus relative-elevation and (E) snow depth versus canopy cover.

Figure 7 shows the soil thermal impact of the 2021 rain event on example locations from each microtopographic group. Hummock and hollow locations experienced short-term perturbations in soil temperature where temperatures briefly warmed and then returned to near-linear rates of seasonal warming (figures 7(B) and (E)). At transition location #1, soil temperatures between 40–140 cm increased from 0 °C to <1 °C positive temperatures while soils at 20–30 cm depths remained ⩽0 °C (figure 7(C)). Transition location #2 had a greater response than transition location #1. Soils between 20–120 cm depth at transition location #2 warmed from ⩽0 °C to 1 °C–4 °C (figure 7(D)). Transition location #2 had a greater proportion of surrounding higher elevation area than transition location #1. In the context of hydrologic flow, the proportion of surrounding higher elevation area can be represented as the ratio of area contributing recharge to lower elevations ($Area_C$,) to area receiving recharge ($Area_R$). Transition location #1 had 2 m^2 of contributing area per 1 m^2 of receiving area leading to an $Area_C$:$Area_R$ ratio of 2:1, while transition location #2 had 6 m^2 of contributing area per 1 m^2 of receiving area leading to an $Area_C$:$Area_R$ ratio of 6:1. Observed responses of all example locations were similar in 2022 (SI figure S3). Soil temperature figures, thermal data, and environmental data for all site locations are available in SI sections S5-S19.

Near-surface (top 10 cm) soil water content of the instrumented hummock location decreased by 0.1 ± 5.0% (<1% change) during the 5.4 cm rain event in 2021 and increased by 9.1 ± 5.5% (29% change) during the 7.7 cm rain event in 2022 (figure 8(A), table 1). Near-surface water content of the instrumented transition location increased by 0.7 ± 5.8% (2% change) and 3.5 ± 4.4% (9% change) during the 2021 and 2022 rain events, respectively (figure 8(B), table 1). In the hollow locations, the

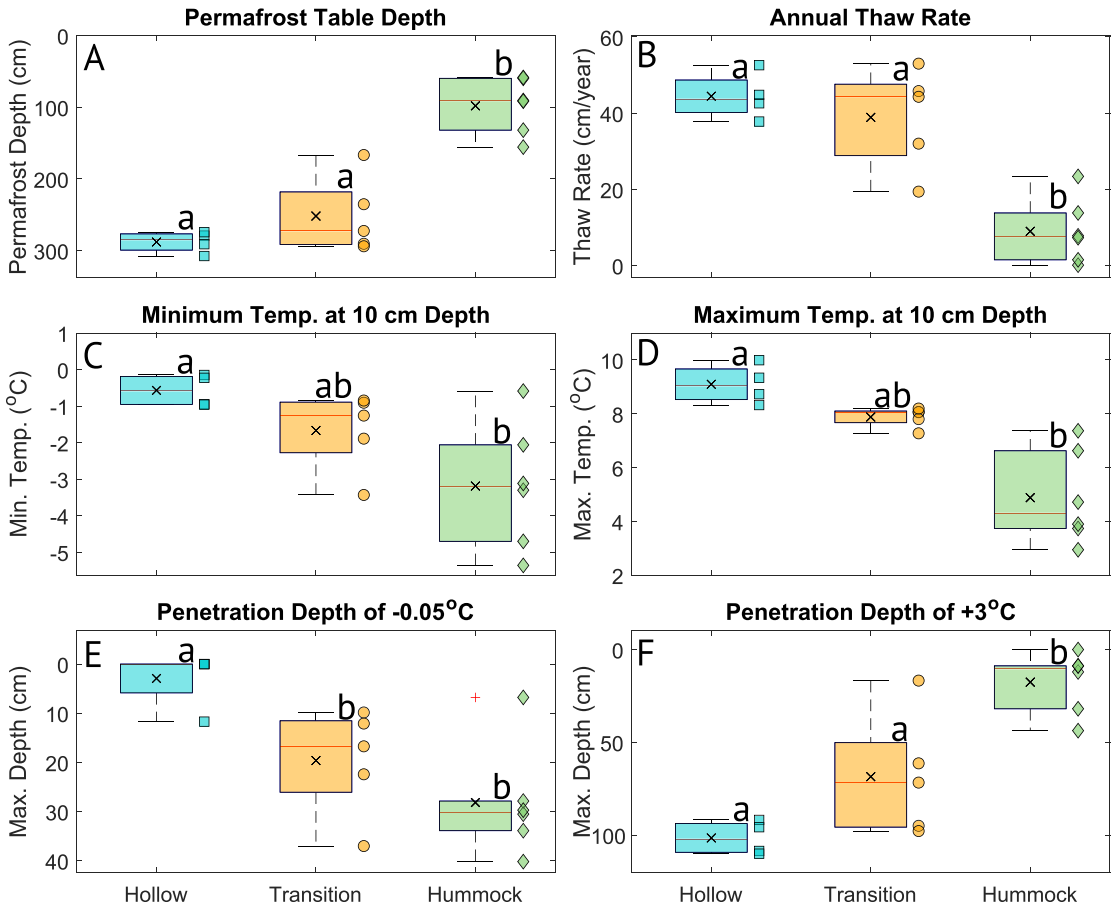

Figure 5. Permafrost progression and thermal metrics among relative-elevation groups. Box and whisker plots showing: (A) Depth to the permafrost table measured on 9 September 2022, (B) average annual deepening of the permafrost table between 2020 and 2022, (C) minimum and (D) maximum temperature reached at a depth of 10 cm between 2020 to 2022, (E), (F) maximum penetration of (E) −0.5 °C and (F) +3 °C. Boxplot statistics described in figure 4.

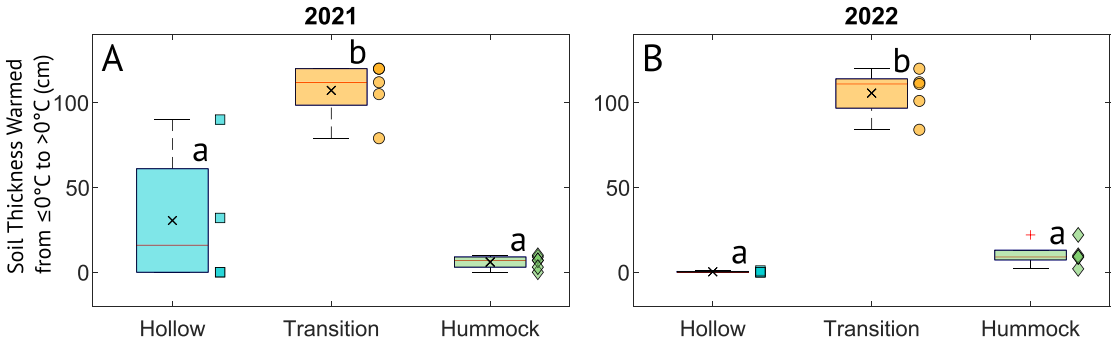

Figure 6. Thermal response to rain among microtopographic groups. Box and whisker plots showing: (A), (B) soil profile thickness of hollow, transition, and hummock locations that warmed from ⩽0 °C to above-freezing temperatures from one week before the largest rain event of the year to one week after the conclusion of the rain event in (A) 2021 and (B) 2022. Boxplot statistics are described in figure 4.

water table moved closer to the land surface by 12.6 ± 3.2 cm (60% change) and 12.8 ± 2.1 cm (62% change) on average during the two rain events (figure 8(C), table 1).

Before the rain events, the hummock location had an estimated thermal conductivity of 0.265 ± 0.044 W $m^{-1}K^{-1}$ in 2021 and 0.244 ± 0.053 W $m^{-1}K^{-1}$ in 2022 (table 1). Estimated pre-event thermal conductivity for the transition location ranged from 0.263 to 0.627 W $m^{-1}K^{-1}$ and 0.287–0.556 W $m^{-1}K^{-1}$ in 2021 and 2022, respectively (table 1). This range was due to uncertainty associated with ice content (see methods 2.6). Soil moisture was not logged at hollows, so thermal conductivity could not be calculated. Due to presumably high soil moisture, hollow locations likely had greater near-surface thermal conductivity than transition or hummock locations.

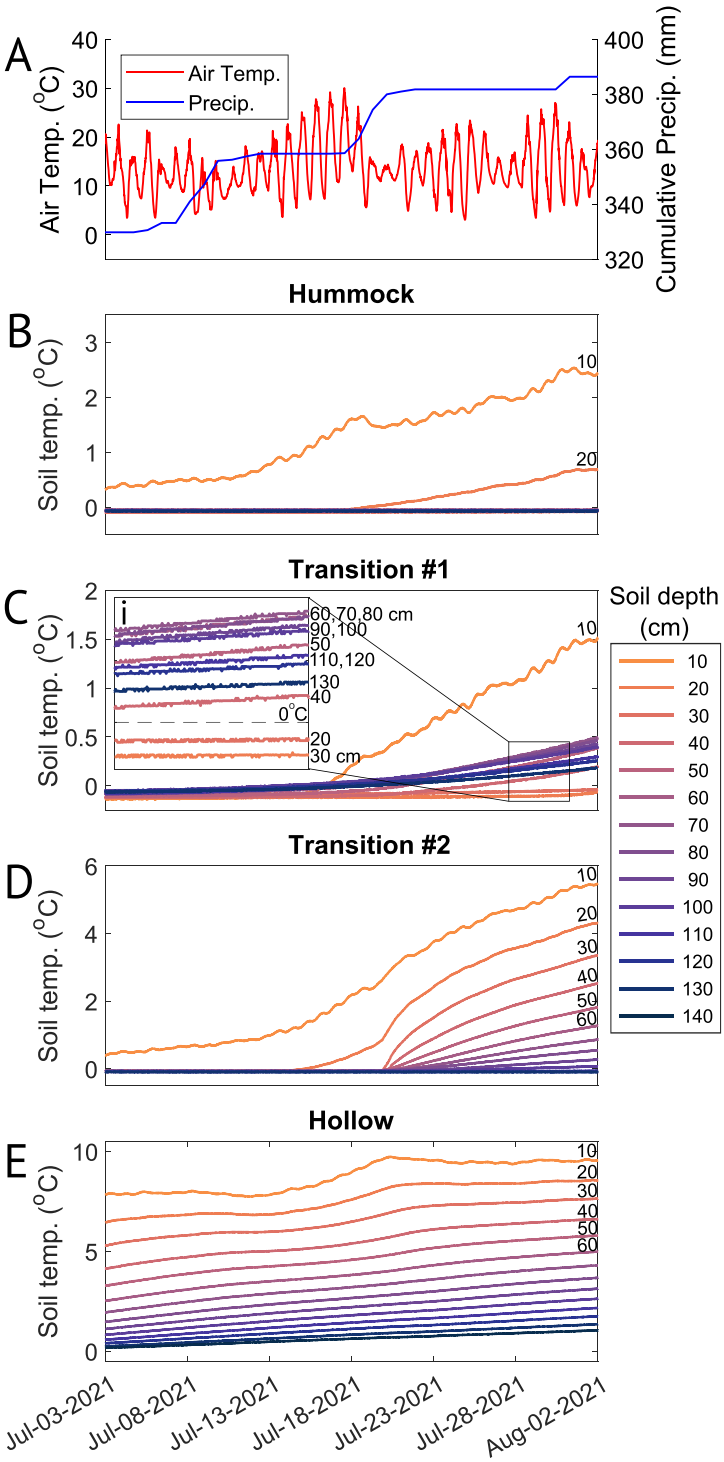

Figure 7. Soil temperature responses to the rain event in July 2021. (A) Air temperature (red, left axis) and cumulative precipitation (blue, right axis). (B)–(E) Soil temperature at depths from 10 to 140 cm below the soil surface (depths are labeled on the figure and colored according to the legend) for (B) hummock location, (C) transition location #1 with zoomed inset (i), (D) transition location #2, and (E) hollow location. The hummock location and transition location #1 were instrumented with soil moisture sensors, see figure 8. *Y*-axis scales vary by location.

Hummock thermal conductivity remained unchanged during the 2021 rain event and increased to 0.297 ± 0.069 W $m^{-1}K^{-1}$ (22% change) during the 2022 event (table 1). Thermal conductivity of the transition location converged to within 1% of the hummock location after the 2021 event (0.267 ± 0.071 W $m^{-1}K^{-1}$) and within 5% after the event in 2022 (0.307 ± 0.061 W $m^{-1}K^{-1}$). Possible changes in transition-location thermal conductivity due to the rain events ranged from a decrease of 45%–57% (high pre-event ice content) to an increase of 1%–7% (ice-free).

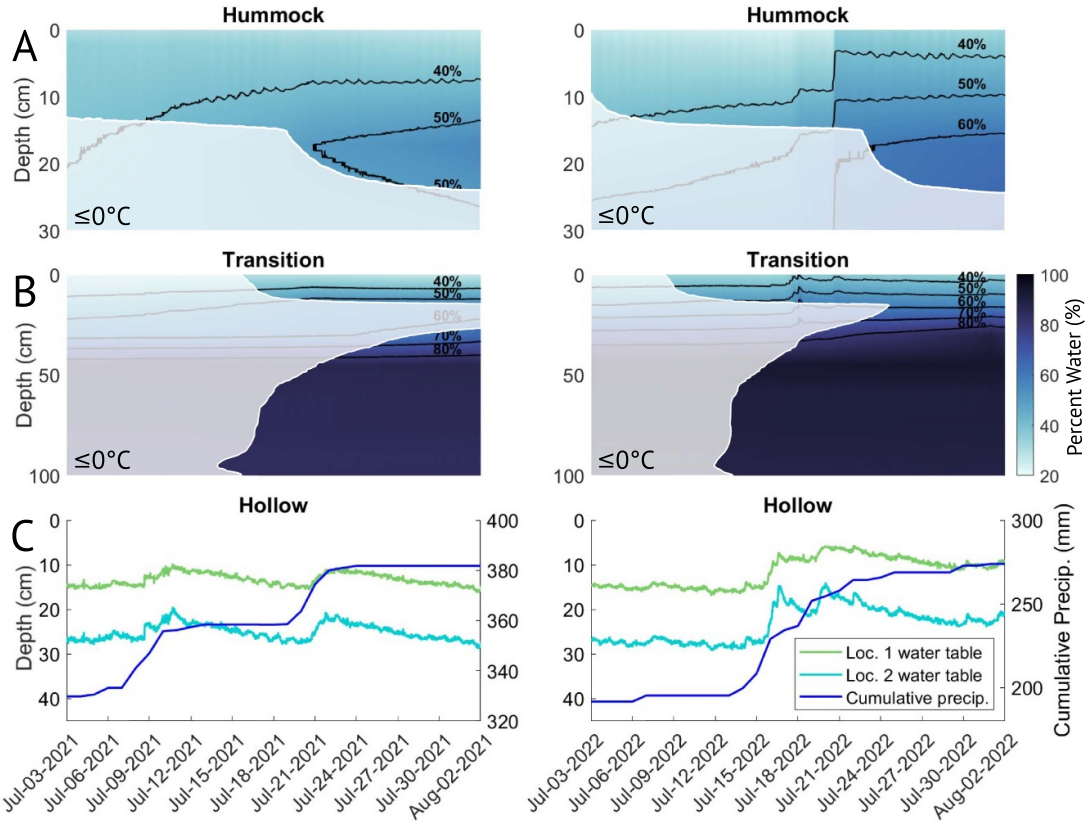

Figure 8. Hydrologic response to rain events in July 2021 (left column) and July 2022 (right column). Colormap plots show soil moisture as percent water for: (A) hummock location and (B) transition location, which are the hummock and transition #1 locations in figure 7(B), (C). A transparent white mask shows areas with a soil temperature of ⩽0 °C. (C) Water table depth of two hollow locations (green and light blue, left axis) and cumulative precipitation (dark blue, right axis). *Y*-axis scales vary by location.

Table 1. Average depth to water table (WT), near-surface water content (θ), and near-surface thermal conductivity (λ) in response to July 2021 and 2022 rain events. Change in depth to water table is averaged for two hollow locations (see figure 8(C)). Soil moisture and thermal conductivity values are average values for soil between 0 and 10 cm from one transition and one hummock location before (3 July) and after (2 August) the rain events in 2021 and 2022 (see figures 8(A) and (B)). Thermal conductivity values of soils at ⩽0 °C are given as a range corresponding to maximum and minimum potential ice content (see methods 2.6). Standard deviations are given for average values.

Event timing	Hollow WT depth (cm)	Transition θ (% water)	Hummock θ (% water)	Transition λ (W m^{-1}K^{-1})	Hummock λ (W m^{-1}K^{-1})
Pre-2021 Event	21.1 ± 8.8	34.6 ± 3.1	35.0 ± 2.2	0.263–0.627	0.265 ± 0.044
Post-2021 Event	14.6 ± 6.8	35.3 ± 5.8	34.9 ± 5.0	0.267 ± 0.071	0.265 ± 0.065
2021 Event Change	12.6 ± 3.2 (60% shallower)	0.7 (2%)	−0.1 (0%)	−0.360 (−57%) to 0.004 (1%)	−0.001 (0%)
Pre-2022 Event	20.6 ± 8.7	38.7 ± 3.6	31.4 ± 3.4	0.287–0.556	0.244 ± 0.053
Post-2022 Event	9.8 ± 5.9	42.3 ± 4.4	40.5 ± 5.5	0.307 ± 0.061	0.297 ± 0.069
2022 Event Change	12.8 ± 2.1 (62% shallower)	3.5 (9%)	9.1 (+29%)	−0.249 (−45%) to 0.020 (7%)	0.053 (+22%)

4. Discussion

4.1. Accelerated thaw due to consecutive rainy and snowy years

As noted in the results, our study captured notably wet and snowy years (figure 2) accompanied by a nine-fold increase in thaw rates along the across-site transect (figure 3) which expanded existing taliks. These taliks begin isolated, progress to connected taliks, and mature into flow-through taliks (Devoie *et al* 2021). Flow-through taliks that are hydrologically connected to wetlands often experience enhanced thaw that is nearly irreversible (Sjöberg *et al* 2016, Devoie *et al* 2019). This process could partially explain rapid thaw observed at the wetland-plateau interface (figure 3).

Hummock locations thawed slowly (figure 5(B)) during the study period while all other locations, including the across-site transect which contained no hummock locations, thawed rapidly (figures 3 and 5(B)). This outcome emphasizes the stability of hummock locations and susceptibility of transition

and hollow locations to rain and snow (figure 5(B)). Increased thickness of taliks, which accompanied permafrost thaw at most site locations, has biogeochemical consequences such as increased methane emissions (Heslop *et al* 2015, O'Neill *et al* 2020), thermal consequences such as greater thaw rates (Connon *et al* 2018, Devoie *et al* 2019), and hydrologic consequences including increased connectivity (Connon *et al* 2018, Devoie *et al* 2019, 2021).

It is known that rain and snow accelerate thaw. During three rainy and snowy years like our site experienced, Iijima *et al* (2010) observed a transition from permafrost stability to thaw ($\sim$5 cm yr^{-1}) at a colder ($-$8 °C MAAT) discontinuous permafrost site. Especially rainy years accelerated observed thaw rates in Interior, AK (Douglas *et al* 2020), and rain from a single wet summer increased thaw for multiple years at a Siberian tundra site (Magnússon *et al* 2022). Seasonally frozen layer thickness has been shown to increase with snow depth in both field (Johansson *et al* 2013, O'Neill and Burn 2017) and modeling (Zhou *et al* 2013, Park *et al* 2015) studies. At our site, locations with greater snow depth (figure 4(C)) thawed more rapidly (figure 5(B)), supporting the notion that snowy conditions between 2020 and 2022 exacerbated permafrost degradation. Composite effects of consecutive wet and snowy years likely contributed to the observed increase in thaw.

4.2. Transition locations thawed rapidly due to advective heat transport by rain

Over 100 cm of above-permafrost transition soil warmed from $\leqslant$0 °C to $>$0 °C during individual rain events in 2021 and 2022 (figures 6, 7(C) and (D)). Two potential mechanisms of rain-induced energy transport could have caused this warming: increased soil thermal conductivity due to increased soil moisture (Farouki 1981, Hinkel and Nelson 2003, Subin *et al* 2013) and advective heat transport (Iijima *et al* 2010, Neumann *et al* 2019, Douglas *et al* 2020, Mekonnen *et al* 2021, Magnússon *et al* 2022).

Increased thermal conductivity due to increased soil moisture does not appear to be the dominant mechanism. Soil-atmospheric thermal interactions are controlled by near-surface thermal conductivity (El-Din 1999). Transition-location thermal conductivity likely decreased during the rain events. Depending on pre-event ice content, the instrumented transition location experienced between a $\sim$57% decrease and $\sim$7% increase in near-surface thermal conductivity (table 1). Regardless, there was no evidence of increased top-down warming or thaw during the rain events (figures 7(C) and 8(B)). During the 2021 event, soils at 20 to 30 cm depth of transition location #1 remained $\leqslant$0 °C while soils from 40 to 140 cm warmed (figures 7(C) and 8(B)). Thus, our data indicates a mechanism that enhances deep soil warming, as opposed to enhancing surface soil-atmospheric energy transport, is responsible for the observed warming and thaw at transition locations.

The pattern of warming and thaw indicates advective heat transport as the primary mechanism. Rain temperature, to a first approximation, is the same as air temperature (Byers *et al* 1949). When rain temperature is greater than soil temperature, rain events can add thermal energy to soil through thermal conduction, rapidly warming soils (Neumann *et al* 2019). During the large July rain events, air temperature was substantially warmer than soil temperature at hummock and transition locations, and slightly warmer than hollow-location soil (figure 7). Transition locations presumably received runoff from surrounding higher-elevation hummocks and released water into lower-elevation hollows. Subsurface runoff increases energy available for warming and thaw, explaining why transition locations warmed during rain events, but hummocks, which did not receive runoff, did not experience enhanced warming. Once flow-limiting soil ice melted within transition locations, subsurface runoff flowed into taliks, warming deeper soil layers. Hollow locations received runoff, but had warm soils before rain events, which minimized the soil-runoff thermal gradient.

Energy contributed by advective heat transport depends on runoff water temperature and volume, while energy needed to warm and thaw soils depends on pre-event soil temperature, water content, and ice content. A key relationship that connects energy contributed to energy needed in this context is the ratio between the land area contributing runoff ($Area_C$) to the land area receiving runoff ($Area_R$). The contributing area influences the volume of runoff generated while the receiving area influences the volume of water and ice that must be warmed and thawed. Transition location #1, which had an $Area_R$:$Area_C$ ratio of 1:2, had a smaller magnitude thermal response to rain (figure 7(C)) than transition location #2 (figure 7(D)), which had a ratio of 1:6. The larger $Area_R$:$Area_C$ ratio of transition location #2 presumably corresponded with relatively greater runoff volume, and therefore, more energy for warming and thaw.

Figure 9 explores the ability of runoff from rain to cause the observed transition location warming and thaw. During these events, $\sim$100 cm of soil with 86% water content (figure 8(B)) and an unknown amount of ground ice warmed from from 0 °C to 1 °C (SI section 1, figures 7(C) and (D)). Since runoff temperature and ice content were unknown quantities, ranges of these values were used as figure axes (figure 9). Minimum and maximum possible runoff temperatures range from the minimum observed event soil temperature, 0 °C, to the average air temperature during the event, 15 °C. At the site, $Area_R$:$Area_C$ varied from 1:2 to 1:6, depending on

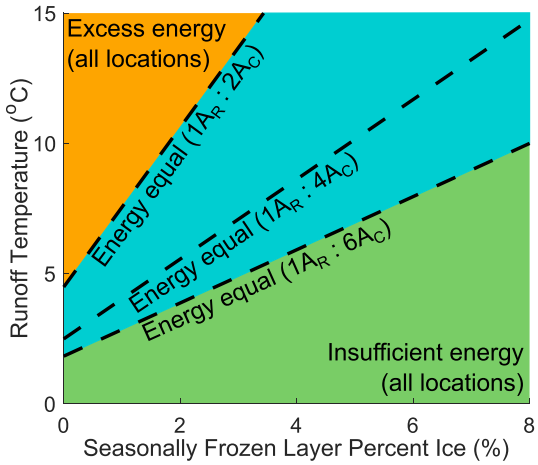

Figure 9. Energy analysis of rain-induced warming and thaw. Dashed black lines mark scenarios where the energy stored in runoff is equal to the energy needed to warm and thaw 100 cm of transition-location soil for ratios of soil area receiving runoff ($Area_R$) to soil area contributing runoff ($Area_C$) of 1:2, 1:4, and 1:6. Below each line, the observed amount of warming is not possible with energy solely from runoff. Above each line, there is a surplus of energy. In the orange region, all scenarios have excess runoff energy. In the green section, all scenarios had insufficient energy to cause the oberved warming and thaw. In the blue region, some scenarios have surplus energy while others have insufficient energy based on $Area_R$:$Area_C$ ratio. The *x*-axis is the percent ice contained in the seasonally frozen layer of transition-location soil. The *y*-axis is the temperature of runoff as it reaches the transition location. This analysis assumes a homogeneous soil profile. The full analysis is shown in SI Section 1.

the transition location. Three different $Area_R$:$Area_C$ scenarios are presented in the figure, 1:2, 1:4, and 1:6 (figure 9). Along each scenario line, energy in subsurface runoff equals energy required for the observed warming and thaw. Above each line, there is a surplus of runoff energy. Below each line, there is insufficient energy to cause the observed warming and thaw. In the orange figure section, all $Area_R$:$Area_C$ scenarios had excess energy. In the blue section, some scenarios had excess energy while others had insufficient energy. In the green section, all scenarios had insufficient energy. See SI section 1 for a full calculation description.

Figure 9 calculations confirm that energy in rain-induced subsurface runoff was sufficient to cause the observed warming and thaw if average ground ice content was low. Using the average $Area_R$:$Area_C$ ratio of 1:4 and an estimated runoff temperature of 7.5 °C, our analysis suggests sufficient energy to warm and thaw 100 cm of soil containing an average of 1.5% ground ice from 0 °C to 1 °C. Runoff temperature was estimated as 7.5 ± 5 °C by mass averaging known masses of 1 °C hummock soil water and 15 °C rainwater. Since all above-permafrost soil except the ~45 cm seasonally frozen layer is ice-free talik (Jones *et al* 2016), ice content is not homogeneously distributed, but concentrated in the top 45 cm of the soil profile. With ice constrained to the seasonally frozen layer, energy from the same 1:4 $Area_R$:$Area_C$ ratio and 7.5 °C runoff was sufficient to warm and thaw 100 cm of soil containing 3.5% of average ground ice in the seasonally frozen layer. The highest observed $Area_R$:$Area_C$ ratio of 1:6, coupled with a 7.5 °C runoff temperature, had sufficient energy to warm and thaw 100 cm of soil with up to 6% of average ground ice in the seasonally frozen layer. Since rain-enhanced thaw depends on runoff, small rain events are not expected to cause notable warming and thaw. To create large-scale advective heat transport, rain events must be sufficiently large to offset losses from evapotranspiration and add sufficient moisture to reach the point of free drainage.

Multiple field and modeling studies have highlighted the ability of rain to enhance warming and thaw (Iijima *et al* 2010, Connon *et al* 2018, Devoie *et al* 2019, 2021, Douglas *et al* 2020, Mekonnen *et al* 2021, Magnússon *et al* 2022), while others have reported a minimal (or cooling) impact (Hamm and Frampton 2021, Gao and Coon 2022). The ability of a single rain event to cause soil warming through advective heat transport has been shown in a wetland environment (Neumann *et al* 2019). Our study highlights the impact of a single rain event on warming and thaw of a warm permafrost plateau containing taliks. Transition locations, which our results indicate are vulnerable to the thermal inputs from rain, are highlighted in dark red and labeled as 'Rain Enhanced Thaw' in figure 10, which presents a conceptual overview of factors affecting permafrost thaw at our site.

4.3. Hummock and hollow location thaw was controlled by canopy cover and microtopography

During our study, hummock locations thawed gradually (8 ± 9 cm yr^{-1}) while hollow locations thawed rapidly (44 ± 6 cm yr^{-1}) (figure 5(B)). Observed hummock soil temperatures were always colder than hollow temperatures (figures 5(C) and (D)), with cold temperatures reaching deeper depths at hummock locations during the cold-season (figure 5(E)), and warm temperatures unable to deeply penetrate during the warm-season (figure 5(F)). These temperature regimes were expected since hollow locations had deeper snow (figure 4(C)) and wetter soils (table 1) than hummock locations, both known causes of warming and thaw (Johansson *et al* 2013, Zhou *et al* 2013, Park *et al* 2015, O'Neill and Burn 2017, Douglas *et al* 2020, Mekonnen *et al* 2021, Magnússon *et al* 2022). Thus, in figure 10, hummock locations are represented as, 'Slow Thaw,' while hollow location areas are labeled, 'Established Area of Thaw.'

Our data indicate snow depth and soil moisture were controlled by canopy cover and relative-elevation, which varied significantly between hummock and hollow locations (figures 4(A) and (B)). Canopy can reduce snow depth through interception of snowfall and contribution of

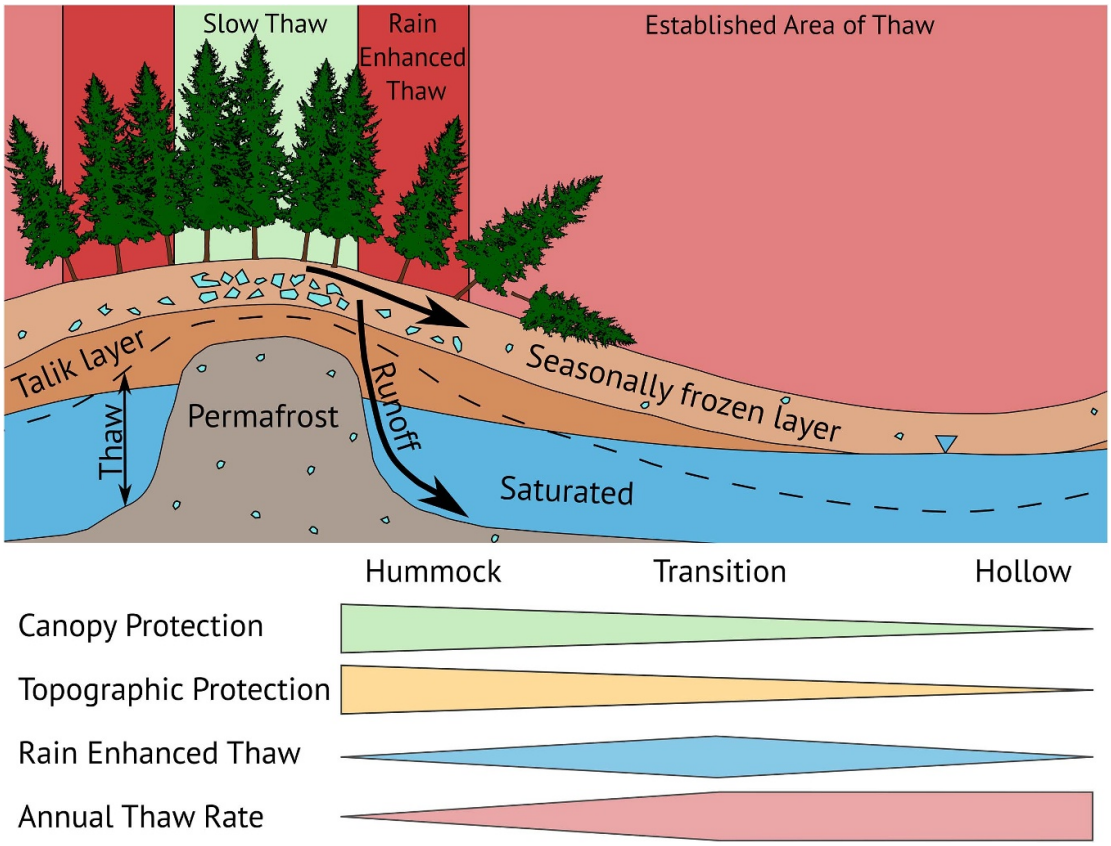

Figure 10. Conceptual overview. The top section shows a permafrost plateau cross-section. Light red represents areas expected to thaw rapidly with or without large rain events, and dark red represents areas only expected to thaw rapidly in the presence of large rain events. Light blue geometric shapes represent soil ice content. A blue triangle marks the top of the water table. Thick black arrows show subsurface flow paths of rain-induced runoff that can warm soil through advective heat transport. A thin black arrow shows the thaw that took place between 2020 and 2022. A dashed black line represents the depth to permafrost before 2020. The seasonally frozen layer is shown in light tan, the talik layer is shown in dark tan, and permafrost is shown in gray. The bottom section shows the relative magnitude of canopy protection, topographic protection, rain-enhanced thaw, and annual thaw rates among hummock, transition, and hollow locations. Canopy protection and topographic protection refer to the slowing of permafrost thaw caused by dense canopy cover and high relative-elevation, both of which reduce snow depth and soil moisture, which are known to accelerate permafrost thaw (Discussion 4.3).

melt-inducing longwave radiation to snowpack (Woo and Giesbrecht 2000, Lundquist *et al* 2013, Webster *et al* 2016). Microtopography can affect snow depth through accumulation in microtopographic depressions during wind-driven snow transport (Clark *et al* 2011). These relationships are reflected in our data establishing correlations between both canopy and relative-elevation with snow depth (figures 4(D) and (E)). Black spruce can reduce soil moisture through transpiration and direct interception of precipitation (Perron *et al* 2023), and higher relative-elevation locations have reduced soil moisture due to exiting runoff (Engstrom *et al* 2005, Graham *et al* 2022). In this way, dense canopy and high relative-elevation keep hummock locations drier (table 1), and therefore, cooler during the warm-season (figures 5(D) and (F)). These cooling effects from high canopy coverage and high relative-elevation are forms of ecosystem protection and are referred to as 'Canopy Protection' and 'Topographic Protection' in figure 10.

Without topographic variation, canopy cover would theoretically be the primary control on both soil moisture and snow depth. In this scenario, areas with dense canopy would thaw slowly due to lower soil moisture and shallower snow depth, while areas with minimal canopy cover would thaw more rapidly. Low canopy areas would, in turn, subside over time, becoming localized low points that accumulate moisture and snow. These wet depressions would continue to thaw and become wetter until a lack of oxygen due to soil saturation would cause back spruce death (Krause and Lemay 2022), leading to less canopy at topographic low points, and perpetuating the feedback loop (Dearborn *et al* 2021, Haynes *et al* 2021). The eventual result of this theoretical model for landscape progression is a positive correlation between relative-elevation and canopy cover like our site (SI figure S1). Without any black spruce, this scenario would advance more rapidly and uniformly.

4.4. Implications of a warmer and wetter future

Observed warming and thaw at this ecosystem-protected site provides a preview of expected future permafrost progression regimes in more northern

latitudes. Rain-induced energy transport to transition locations provided sufficient energy to cause warming and thaw of low ice-content soil, due in part to hydrologically connected taliks (figures 9 and 10). In the absence of taliks, this mechanism could, over time, cause enhanced thaw and the development of taliks. As larger rain events become more common in northern high-latitudes (Cohen *et al* 2014, Kusunoki *et al* 2015, Liu *et al* 2021, Wang *et al* 2021, Thackeray *et al* 2022), and air temperatures continue to rise (Rantanen *et al* 2022), the energy contribution from this mechanism is expected to increase. This increase, however, is not expected across the entire permafrost zone. Precipitation changes are highly variable across northern high latitudes (Bintanja *et al* 2020). In addition, permafrost sites located in continental climates, such as the semi-continental climate of our site, have been shown to experience the greatest rain-induced warming through a combination of enhanced summer precipitation and warmer summer air temperatures, while maritime climates tend to experience a slight cooling effect from heavy rainfall (Hamm *et al* 2023).

Our analyses indicate the nine-fold increase in thaw rates observed between 2020 and 2022 (figure 3) was facilitated by low ice content and the presence of taliks within the permafrost plateau. Decades of exposure to a MAAT above 0 °C presumably caused permafrost soils to warm, taliks to form, and soil to lose ice content. This prior slow warming allowed energy inputs from three snowy and wet years, and two large warm-season rain events, to overcome the low remaining resistance to thaw. As temperatures in northern high-latitudes continue to warm more quickly than the global average (Rantanen *et al* 2022), causing more of the permafrost zone to experience mean annual temperatures above 0 °C, more permafrost will likely experience reduced ice content and become vulnerable to similar rapid thaw events. For example, in response to increased winter precipitation and snow at a colder and more stable site in northern Sweden, Webster *et al* (2016) observed permafrost soils warm while the late-season thaw depth remained relatively stable. This site is now more vulnerable to the type of future thaw observed at our site.

5. Conclusion

Based on high-resolution soil temperature data, repeat permafrost surveys, and measurements of environmental variables, we determined that the thaw of our ecosystem-protected permafrost site, and expansion of taliks, accelerated nine-fold during three consecutive wet and snowy years. Neither thaw rates, nor mechanisms of thaw, were uniform across the site. Hummock locations experienced only 8 ± 9 cm yr^{-1} of thaw, while hollow and transition locations thawed 44 ± 6 cm yr^{-1} and 39 ± 13 cm yr^{-1}, respectively (figure 5(B)). Mechanisms of thaw between hollow and transition locations differed. Hollow locations had high thermal conductivity due to high soil moisture (table 1) and ample cold-season insulation from deep snow (figure 3(C)), while transition locations experienced substantial warming and thaw from thermal energy transported through subsurface taliks by runoff during individual rain events (figures 6 and 7(C), (D) and 9). As northern high-latitudes continue to become warmer and wetter, and rain events become more extreme, these observed mechanisms of warming and thaw are expected to increase.

Data availability statement

The data that support the findings of this study are openly available at the following URL/DOI: https://doi.org/10.15485/2204548 (Eklof *et al* 2023).

Acknowledgments

We thank Bill Eklof and Greg Vandas for field assistance, Patrick McClure, Stijn Wielandt, and Chen Wang for assistance with DTPs, and Bruce Chambers for assistance with soil moisture instrumentation. This material is based on work supported, in part, by the U.S. Department of Energy, Office of Science, Office of Biological and Environmental Research under award number DE-SC0019063 and the National Science Foundation under award EAR-2142464. Additional support was provided by Benjamin M Jones through the National Science Foundation Award OIA-1929170, and by Baptiste Dafflon under the Next Generation Ecosystem Experiment (NGEE) Arctic project funded by the U.S. Department of Energy, Office of Biological and Environmental Research under contract DEAC02-05CH11231. Any use of trade, firm, or product names is for descriptive purposes only and does not imply endorsement by the U.S. Government.

ORCID iDs

Joel F Eklof https://orcid.org/0000-0003-4840-834X
Benjamin M Jones https://orcid.org/0000-0002-1517-4711
Baptiste Dafflon https://orcid.org/0000-0001-9871-5650
Élise G Devoie https://orcid.org/0000-0003-1752-8437
Katie M Ring https://orcid.org/0000-0002-4645-621X
Marie E English https://orcid.org/0000-0001-7769-8724
Mark P Waldrop https://orcid.org/0000-0003-1829-7140
Rebecca B Neumann https://orcid.org/0000-0003-3464-9046

References

Beckschäfer P 2015 Hemispherical_2.0—Batch processing hemispherical and canopy photographs with ImageJ—User Manual (https://doi.org/10.1371/journal.pone.0134935)

Beilman D W, Vitt D H and Halsey L A 2001 Localized permafrost peatlands in western Canada: definition, distributions, and degradation *Arct. Antarct. Alp. Res.* **33** 70–77

Bintanja R and Selten F M 2014 Future increases in Arctic precipitation linked to local evaporation and sea-ice retreat *Nature* **509** 479–82

Bintanja R, van der Wiel K, van der Linden E C, Reusen J, Bogerd L, Krikken F and Selten F M 2020 Strong future increases in Arctic precipitation variability linked to poleward moisture transport *Sci. Adv.* **6** eaax6869

Blok D, Heijmans M M P D, Schaepman-Strub G, van Ruijven J, Parmentier F J W, Maximov T C and Berendse F 2011 The cooling capacity of mosses: controls on water and energy fluxes in a Siberian tundra site *Ecosystems* **14** 1055–65

Brown J, Sidlauskas F J and Delinski G 1997 Circum-Arctic map of permafrost and ground ice conditions

Byers H R, Moses H and Harney P J 1949 Measurement of rain temperature *J. Meteorol.* **6** 51–55

Clark M P, Hendrikx J, Slater A G, Kavetski D, Anderson B, Cullen N J, Kerr T, Örn Hreinsson E and Woods R A 2011 Representing spatial variability of snow water equivalent in hydrologic and land-surface models: a review *Water Resour. Res.* **47** W07539

Clayton L K *et al* 2021 Active layer thickness as a function of soil water content *Environ. Res. Lett.* **16** 055028

Cohen J *et al* 2014 Recent Arctic amplification and extreme mid-latitude weather *Nat. Geosci.* **7** 627–37

Connon R, Devoie É, Hayashi M, Veness T and Quinton W 2018 The influence of shallow taliks on permafrost thaw and active layer dynamics in subarctic Canada *J. Geophys. Res. Earth Surf.* **123** 281–97

Dafflon B *et al* 2022 A distributed temperature profiling system for vertically and laterally dense acquisition of soil and snow temperature *Cryosphere* **16** 719–36

Dearborn K D, Wallace C A, Patankar R and Baltzer J L 2021 Permafrost thaw in boreal peatlands is rapidly altering forest community composition *J. Ecol.* **109** 1452–67

Devoie É G, Craig J R, Connon R F and Quinton W L 2019 Taliks: a tipping point in discontinuous permafrost degradation in peatlands *Water Resour. Res.* **55** 9838–57

Devoie É G, Craig J R, Dominico M, Carpino O, Connon R F, Rudy A C A and Quinton W L 2021 Mechanisms of discontinuous permafrost thaw in peatlands *J. Geophys. Res. Earth Surf.* **126** e2021JF006204

Douglas T A, Turetsky M R and Koven C D 2020 Increased rainfall stimulates permafrost thaw across a variety of interior Alaskan boreal ecosystems *npj Clim. Atmos. Sci.* **3** 1–7

Eklof J, Jones B, Dafflon B, Ring K, English M and Neumann R 2023 Soil temperature and soil moisture raw data, permafrost table depths, and accompanying environmental variable data, Kenai Wildlife Refuge, 2019–2022 *Effects of Rapid Permafrost Thaw on CO2 and CH4 Fluxes in a Warmer and Wetter Future, ESS-DIVE repository* (https://doi.org/10.15485/2204548) (Accessed 16 March 2024)

El-Din M M S 1999 On the heat flow into the ground *Renew. Energy* **18** 473–90

Engstrom R, Hope A, Kwon H, Stow D and Zamolodchikov D 2005 Spatial distribution of near surface soil moisture and its relationship to microtopography in the Alaskan Arctic coastal plain *Hydrol. Res.* **36** 219–34

Farouki O T 1981 Thermal properties of soils (Defense Technical Information Center (available at: www.dtic.mil/docs/citations/ADA111734)

Gao B and Coon E T 2022 Evaluating simplifications of subsurface process representations for field-scale permafrost hydrology models *Cryosphere* **16** 4141–62

Graham J D, Ricciuto D M, Glenn N F and Hanson P J 2022 Incorporating microtopography in a land surface model and quantifying the effect on the carbon cycle *J. Adv. Model. Earth Syst.* **14** e2021MS002721

Hamm A and Frampton A 2021 Impact of lateral groundwater flow on hydrothermal conditions of the active layer in a high-Arctic hillslope setting *Cryosphere* **15** 4853–71

Hamm A, Magnússon R Í, Khattak A J and Frampton A 2023 Continentality determines warming or cooling impact of heavy rainfall events on permafrost *Nat. Commun.***14** 3578

Harris S A 1988 Glossary of permafrost and related ground-ice terms (Ottawa,Ontario,Canada)

Haynes K M, Smart J, Disher B, Carpino O and Quinton W L 2021 The role of hummocks in re-establishing black spruce forest following permafrost thaw *Ecohydrology* **14** e2273

Heslop J K, Walter Anthony K M, Sepulveda-Jauregui A, Martinez-Cruz K, Bondurant A, Grosse G and Jones M C 2015 Thermokarst lake methanogenesis along a complete talik profile *Biogeosciences* **12** 4317–31

Hinkel K M and Nelson F E 2003 Spatial and temporal patterns of active layer thickness at Circumpolar Active Layer Monitoring (CALM) sites in northern Alaska, 1995–2000 *J. Geophys. Res. Atmos.* **108**

Hinkel K M, Paetzold F, Nelson F E and Bockheim J G 2001 Patterns of soil temperature and moisture in the active layer and upper permafrost at Barrow, Alaska: 1993–1999 *Glob. Planet. Change* **29** 293–309

Iijima Y, Fedorov A N, Park H, Suzuki K, Yabuki H, Maximov T C and Ohata T 2010 Abrupt increases in soil temperatures following increased precipitation in a permafrost region, central Lena River basin, Russia *Permafr. Periglac. Process.* **21** 30–41

Johansson M, Callaghan T V, Bosiö J, Åkerman H J, Jackowicz-Korczynski M and Christensen T R 2013 Rapid responses of permafrost and vegetation to experimentally increased snow cover in sub-arctic Sweden *Environ. Res. Lett.* **8** 035025

Jonas T, Webster C, Mazzotti G and Malle J 2020 HPEval: a canopy shortwave radiation transmission model using high-resolution hemispherical images *Agric. For. Meteorol.* **284** 107903

Jones B M, Baughman C A, Romanovsky V E, Parsekian A D, Babcock E L, Stephani E, Jones M C, Grosse G and Berg E E 2016 Presence of rapidly degrading permafrost plateaus in south-central Alaska *Cryosphere* **10** 2673–92

Juszak I, Erb A M, Maximov T C and Schaepman-Strub G 2014 Arctic shrub effects on NDVI, summer albedo and soil shading *Remote Sens. Environ.* **153** 79–89

Krause C and Lemay A 2022 Root adaptations of black spruce growing in water-saturated soil *Can. J. For. Res.* **52** 653–61

Kusunoki S, Mizuta R and Hosaka M 2015 Future changes in precipitation intensity over the Arctic projected by a global atmospheric model with a 60-km grid size *Polar Sci.* **9** 277–92

Liu J, Wu D, Xu X, Ji M, Chen Q and Wang X 2021 Projection of extreme precipitation induced by Arctic amplification over the Northern Hemisphere *Environ. Res. Lett.* **16** 074012

Loranty M M *et al* 2018 Reviews and syntheses: changing ecosystem influences on soil thermal regimes in northern high-latitude permafrost regions *Biogeosciences* **15** 5287–313

Lundquist J D, Dickerson-Lange S E, Lutz J A and Cristea N C 2013 Lower forest density enhances snow retention in regions with warmer winters: a global framework developed from plot-scale observations and modeling *Water Resour. Res.* **49** 6356–70

Lundquist J D and Huggett B 2008 Evergreen trees as inexpensive radiation shields for temperature sensors: TREES AND TEMPERATURE SENSORS *Water Resour. Res.* **44**

Magnússon R Í, Hamm A, Karsanaev S V, Limpens J, Kleijn D, Frampton A, Maximov T C and Heijmans M M P D 2022a Extremely wet summer events enhance permafrost thaw for multiple years in Siberian tundra *Nat. Commun.* **13** 1556

Mekonnen Z A, Riley W J, Grant R F and Romanovsky V E 2021 Changes in precipitation and air temperature contribute

comparably to permafrost degradation in a warmer climate *Environ. Res. Lett.* **16** 024008
Neumann R B, Moorberg C J, Lundquist J D, Turner J C, Waldrop M P, McFarland J W, Euskirchen E S, Edgar C W and Turetsky M R 2019 Warming effects of spring rainfall increase methane emissions from thawing permafrost *Geophys. Res. Lett.* **46** 1393–401
NOAA 2023 National maps—Alaska—NOAA's national weather service (available at: www.nws.noaa.gov/outlook_ak_tab.php)
O'Donnell J A, Romanovsky V E, Harden J W and McGuire A D 2009 The effect of moisture content on the thermal conductivity of moss and organic soil horizons from black spruce ecosystems in interior Alaska *Soil Sci.* **174** 646–51
O'Neill H B and Burn C R 2017 Talik formation at a snow fence in continuous permafrost, Western Arctic Canada *Permafr. Periglac. Process.* **28** 558–65
O'Neill H B, Roy-Leveillee P, Lebedeva L and Ling F 2020 Recent advances (2010–2019) in the study of taliks *Permafr. Periglac. Process* **31** 346–57
Park H, Fedorov A N, Zheleznyak M N, Konstantinov P Y and Walsh J E 2015 Effect of snow cover on pan-Arctic permafrost thermal regimes *Clim. Dyn.* **44** 2873–95
Perron N, Baltzer J L and Sonnentag O 2023 Spatial and temporal variation in forest transpiration across a forested boreal peatland complex *Hydrol. Process.* **37** e14815
Rantanen M, Karpechko A Y, Lipponen A, Nordling K, Hyvärinen O, Ruosteenoja K, Vihma T and Laaksonen A 2022 The Arctic has warmed nearly four times faster than the globe since 1979 *Commun. Earth Environ.* **3** 1–10
Shur Y L and Jorgenson M T 2007 Patterns of permafrost formation and degradation in relation to climate and ecosystems *Permafr. Periglac. Process.* **18** 7–19
Sjöberg Y, Coon E, Sannel K, B A, Pannetier R, Harp D, Frampton A, Painter S L and Lyon S W 2016 Thermal effects of groundwater flow through subarctic fens: a case study based on field observations and numerical modeling *Water Resour. Res.* **52** 1591–606
Smith S L, O'Neill H B, Isaksen K, Noetzli J and Romanovsky V E 2022 The changing thermal state of permafrost *Nat. Rev. Earth Environ.* **3** 10–23
Subin Z M, Koven C D, Riley W J, Torn M S, Lawrence D M and Swenson S C 2013 Effects of soil moisture on the responses of soil temperatures to climate change in cold regions *J. Clim.* **26** 3139–58
Thackeray C W, Hall A, Norris J and Chen D 2022 Constraining the increased frequency of global precipitation extremes under warming *Nat. Clim. Change* **12** 441–8
USDA 2023 Kenai Moose Pens (966)—site information and reports USDA (available at: https://wcc.sc.egov.usda.gov/nwcc/site?sitenum=966)
Wang P, Huang Q, Tang Q, Chen X, Yu J, Pozdniakov S P and Wang T 2021 Increasing annual and extreme precipitation in permafrost-dominated Siberia during 1959–2018 *J. Hydrol.* **603** 126865
Webster C, Rutter N, Zahner F and Jonas T 2016 Measurement of incoming radiation below forest canopies: a comparison of different radiometer configurations *J. Hydrometeorol.* **17** 853–64
Wielandt S, Uhlemann S, Fiolleau S and Dafflon B 2023 TDD LoRa and delta encoding in low-power networks of environmental sensor arrays for temperature and deformation monitoring *J. Signal Process. Syst.* **95** 831–43
Woo M and Giesbrecht M A 2000 Simulation of snowmelt in a subarctic spruce woodland: 1. Tree model *Water Resour. Res.* **36** 2275–85
Yoshikawa K, Overduin P P and Harden J W 2004 Moisture content measurements of moss (Sphagnum spp.) using commercial sensors *Permafr. Periglac. Process.* **15** 309–18
Zhao Y, Si B, Zhang Z, Li M, He H and Hill R L 2019 A new thermal conductivity model for sandy and peat soils *Agric. For. Meteorol.* **274** 95–105
Zhou J, Kinzelbach W, Cheng G, Zhang W, He X and Ye B 2013 Monitoring and modeling the influence of snow pack and organic soil on a permafrost active layer, Qinghai–Tibetan Plateau of China *Cold Reg. Sci. Technol.* **90–91** 38–52